

Terahertz-driven parametric excitation of Raman-active phonons in LaAlO_3

M. Basini,^{1,2,*} V. Unikandanunni,^{1,3,*} F. Gabriele,^{4,*} M.
Cross,⁵ M. Hoffmann,⁵ F. Forte,⁴ M. Cuoco,⁴ and S. Bonetti^{1,6,†}

¹*Department of Physics, Stockholm University, Stockholm, Sweden*

²*Physics Department, ETH Zürich, Zürich, Switzerland*

³*Institute of Applied Physics, Bern University, Bern, Switzerland*

⁴*CNR-SPIN, Fisciano (Salerno), Italy,*

c/o Università di Salerno, Fisciano (Salerno), Italy

⁵*SLAC National Accelerator Laboratory, Menlo Park, USA*

⁶*Department of Molecular Sciences and Nanosystems,*

Ca' Foscari University of Venice, Venice, Italy

Abstract

Achieving parametric excitation in an oscillating physical system involves periodically adjusting one of its parameters to modulate the oscillator’s natural frequency [1]. This phenomenon has been observed in numerous systems within physics and engineering, profoundly transforming modern science and technology [2–8]. Despite rapid progress, the parametric control of collective excitations, such as phonons, remains a challenge while promising to generate novel and intriguing effects in a largely unexplored field. Here, we investigate the terahertz (THz) field-induced dynamics of Raman-active phonons in LaAlO_3 (LAO), an archetypal quantum material for its electronic and structural properties. Utilizing intense THz pulses, we demonstrate a novel mechanism of parametric phonon excitation marked by substantial subharmonic components. Theoretical analysis can successfully capture the hallmarks of the observed phenomena in a physical scenario with the THz field inducing a parametric coupling between the Raman mode and pairs of acoustic phonon excitations.

Parametric excitation and associated devices play a crucial role in enhancing weak electromagnetic signals [2–4], facilitating the conversion of collective modes between different frequencies [5–7], generating and measuring squeezed and entangled states [9–11], and enabling the development of innovative information processing architectures [8]. When brought to the realm of sound waves, the parametric control, generation, and manipulation of phonons have long been sought after, presenting unparalleled opportunities to advance the field of phononics [7, 12–16]. In this framework, the attention has been mostly devoted to the realization of materials platforms and devices for the amplification of phonons in low-frequency range (e.g. trapped ions [17–19], optical tweezers [20] and nanomechanical resonators [21–23]), as well as for terahertz phonons in semiconductor superlattices [24] and by means of pump-probe experiments in SiC [25]. Although significant advancements have been made, parametric controlling of collective excitations like phonons remains a challenge.

In this work, we present evidence of a yet unexplored mechanism for a coherent parametric excitation of low-energy Raman-active phonon in the centrosymmetric lanthanum aluminate, LaAlO_3 (LAO), which makes use of an intense THz electric field. So far the excitation of Raman-active modes in solids have been achieved directly via inelastic scat-

* These authors contributed equally

† Corresponding author

tering of light, i.e., Electronic Raman Scattering (ERS) [26], or indirectly via Ionic Raman Scattering (IRS) [27–31], where infrared-active phonons mediate the scattering process that results in the excitation of a Raman-active phonon. Here, we demonstrate that an intense terahertz pulse, with central frequency in the range of 1-2 THz, not only has the ability to coherently stimulate the Raman-active E_g phonon at about 1 THz but also generates significant subharmonic spectral components, which are distinct signatures of an underlying parametric-driving mechanism. This mechanism is based on the absorption of photons through an optical transition involving a pair of acoustic vibrational modes. The interaction between the Raman-active and the acoustic modes results in a parametric excitation of the Raman-active phonon, leading to the emergence of dynamical components at subharmonic frequencies.

LAO is a versatile material: as a single bulk crystal is commonly used as a substrate for the epitaxial growth of other perovskite oxides, and, as a thin film, it constitutes a building block for heterostructures and devices based on functional interfaces [32]. LAO is a wide gap insulator ($E_{\text{gap}}=6.1$ eV), with a perovskite structure that undergoes a cubic $R\bar{3}c$ to rhombohedral $Pm\bar{3}m$ phase transition at $T = 813$ K, associated with the rotation of the AlO_6 octahedra in anti-phase about the pseudocubic [111] axis [33]. At the same temperature, the material becomes ferroelastic [34, 35]. For our experiments, we use a double-side polished LaAlO_3 [100] bulk crystal with a thickness of 0.5 mm. The material’s nonlinear optical response is measured in a pump-probe experimental configuration, where the pump used is either a near-infrared (1300 nm) or broadband single-cycle terahertz radiation. The near-infrared radiation is generated via optical parametric amplification of a 40 fs-long pulse centered at 800 nm wavelength, produced by a 1 kHz Ti:Sapphire amplifier. The wavelength and pulse duration of the near-infrared pump are 1300 nm and, respectively, 60 fs. Broadband (0.5 - 3THz) single-cycle terahertz radiation is generated by optical rectification of the same near-infrared laser pulse in the organic crystal OH1 [36]. The terahertz pulses were then focused on the sample using parabolic mirrors to a maximum field amplitude of 700kV/cm. We use a pair of wire-grid polarizers to control the amplitude of the THz field for conducting field-dependence measurements. The electro-optical sampling of the generated THz electric field is shown in the Extended Data. The probe pulses are produced by the same 1 kHz amplifier used to generate the pump radiation. The geometry of the pump and probe setup is shown in Figure 1a. A half-wave plate together with a Wollaston prism is

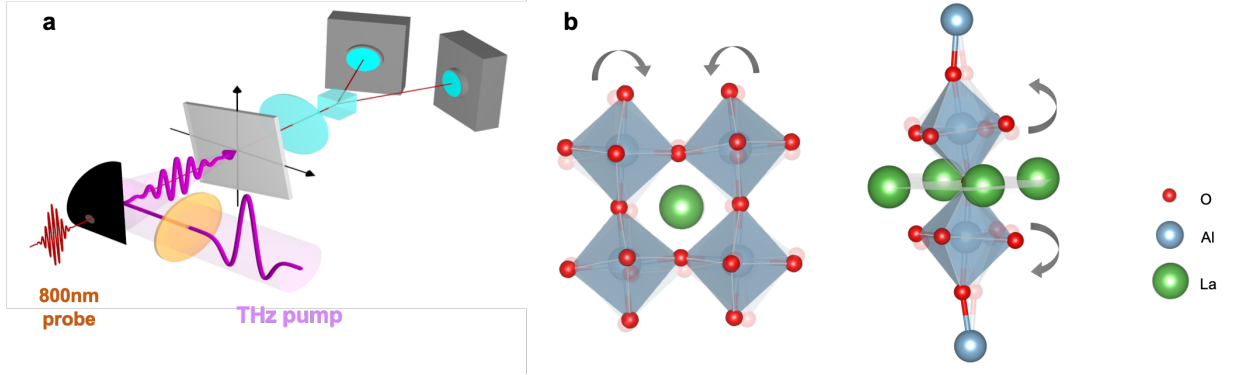


Figure 1. **Sketches of the experiment and of LaAlO_3 unit cell and phonon dynamics.**

(a) Schematic of the pump-probe setup used in this study. (b) LaAlO_3 crystal structure in the rhombohedral phase and atomic displacements involved in the E_g mode

used to implement a balanced detection scheme with two photodiodes.

The measurements are performed at 8K, the temperature at which the material is centrosymmetric with a rhombohedral unit cell. Figure 2 shows the signal arising from the polarization rotation of the probe beam transmitted by the sample after its excitation. To facilitate the comparison between near-infrared and THz excitations, the sample response was normalized on the incident pump fluence. A long-lasting vibration is visible in Fig. 2(a), which illustrate the pump-probe, time domain data for both pump wavelengths. Fig. 2(b) plots the Fast Fourier Transform (FFT) of the same time-domain signal. The FFT data is dominated by a narrow peak, whose central frequency, 1.08 THz is comparable to one of the lower frequency Raman active modes of LaAlO_3 , i.e. the anti-distortive phonon mode with E_g symmetry [37]. As illustrated in Fig. 1(b), the atomic displacements of the mode are associated with the oxygen octahedra rotation about the pseudocubic axes [111].

The data presented in Fig. 2 demonstrate that both the 1300 nm and the broadband terahertz pumps are capable of exciting the E_g mode in the material. Furthermore, when excited with a broadband terahertz field, the material response exhibits low-frequency spectral components: a quasi-continuum below 1 THz, with a well-defined peak at 0.34 THz, which has not been reported previously. These low-frequency spectral components are not observed when driving the system with the 1300 nm pump. To gain a deeper insight on these features and the excitation mechanism, we measured the THz response of the system after inserting two band-pass filters, at 1 and 2 THz, before the sample. These additional

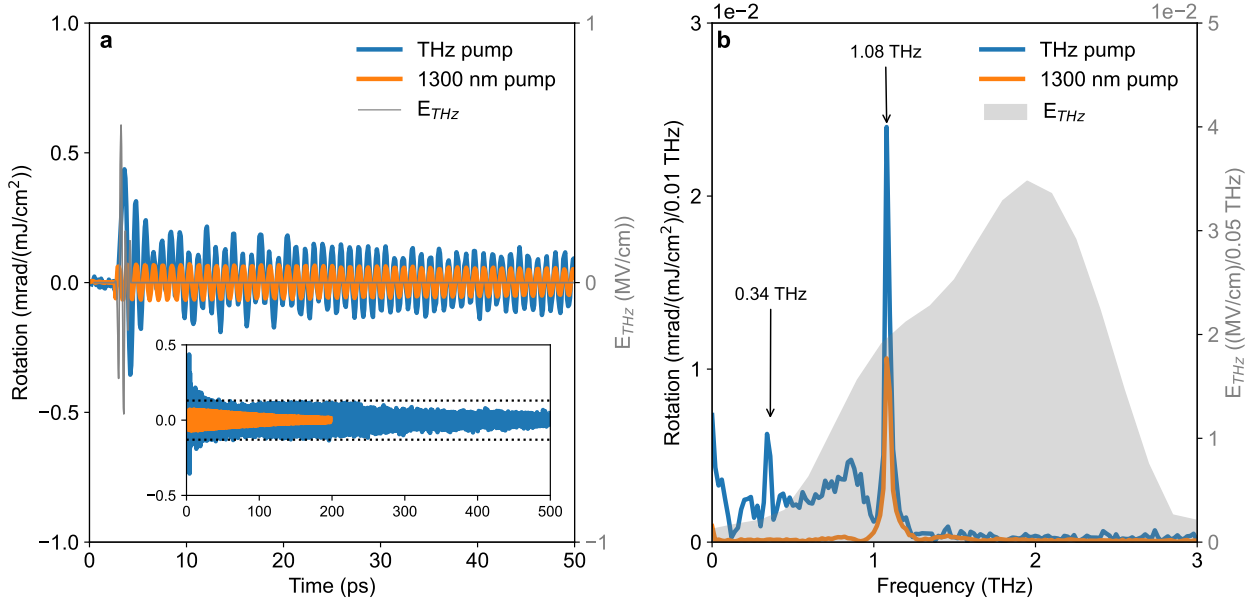


Figure 2. **Experimentally detected polarization rotation in LaAlO₃ following near-infrared or THz pumps.** Polarization rotation of a transmitted 800 nm probe through a LaAlO₃ crystal, following the excitation by a near-infrared (1300nm) (orange curve) or a broadband THz excitation (blue curve), in (a) time and (b) frequency domains. Measurements are performed at 8 K. The FFT is evaluated in the range of 0-50 ps. The sample response is normalized by the pump fluence. Inset in panel (a): time-domain dynamics at longer timescales.

data are shown in the Supplementary Information.

Building on the previous experimental evidences, we now identify the potential excitation pathway responsible for the emergence of both the E_g and low-frequency peaks in the sample response. The field dependence of the E_g peak, analyzed in detail in S2 of the Supplementary Information, exhibits a quadratic trend, providing evidence that the same mode is excited via the impulsive stimulated version of the electronic Raman scattering (ISRS) [38]. Nevertheless, such an excitation mechanism does not account for the THz-driven low-frequency optical response. The experimental observation of sub-harmonic peaks emerging alongside the E_g mode, and the lack of optical phonons and electronic excitations below 1 THz, point instead towards a novel physical scenario involving THz-field driven parametric excitation of the Raman-active phonon mode. Such a scenario can be captured by a phenomenological model, wherein light triggers two acoustic phonon modes (Q_{ac}) that are subsequently

converted into two Raman-active phonon modes (Q_R), as sketched in Fig. 3. The relevant symmetry-allowed terms in the expansion of the potential are

$$\begin{aligned}
V(Q_R, Q_{ac}) = & \frac{\Omega_R^2}{2} Q_R^2 + \sum_{\mathbf{q}} \frac{\Omega_{ac}(\mathbf{q})^2}{2} Q_{ac}(-\mathbf{q}) Q_{ac}(\mathbf{q}) \\
& - \frac{Z_{ac}}{2} \sum_{\mathbf{q}} Q_{ac}(-\mathbf{q}) Q_{ac}(\mathbf{q}) E_{ext}^2(t) + \frac{d}{4} \sum_{\mathbf{q}} Q_{ac}(-\mathbf{q}) Q_{ac}(\mathbf{q}) Q_R^2, \quad (1)
\end{aligned}$$

where the first row describes the Raman-active and the acoustic phonons oscillating with respective frequencies Ω_R and Ω_{ac} in the harmonic approximation, the second row describes the simultaneous excitation of two acoustic phonons with opposite momenta, mediated by the effective charge Z_{ac} , and the acousto-optic conversion, controlled by the coefficient d . The THz pump field is modeled as $E_{ext}(t) = E_0 F(t) \cos(\Omega_{pump} t)$. In this effective model, the focus is near the Γ -point, where we implicitly introduce a momentum cutoff k_{cut} smaller than the Debye wave-vector $k_D \sim 1.0 \text{ \AA}^{-1}$ associated with phonons in LAO. For $|\mathbf{q}| < k_{cut}$, indeed, the Raman-active phonon exhibits a nearly flat dispersion, resulting in a sharply peaked density of states. Consequently, we also approximate Z_{ac} and d as constant within this momentum range. Eq. (1) leaves out, for simplicity, the ISRS mechanism, which enters the phonon potential with a term $E_{ext}^2 Q_R$ and, as mentioned before, directly drives the E_g mode without impacting the subharmonic spectrum. This term sets the initial condition for the phonon's equation of motion, as detailed in the Supplementary Information.

By integrating out the acoustic modes (see Supplementary Information for the explicit derivation) and rescaling the time variable with respect to the Raman frequency Ω_R , one finds that the dynamics of the Raman-active phonon, that from now on we denote by x for simplicity, is described, in the case of an ultrashort pump pulse with envelope $F(t) = \delta(t)$, by the following Mathieu's equation,

$$\ddot{x}(t) + [1 + \delta \cos(\omega t)] x(t) = 0. \quad (2)$$

Eq. (2) describes the parametric driving of the Raman-active phonon, with a parameter δ (see Supplementary Information for its explicit definition), at $\omega \equiv 2\Omega_0/\Omega_R$. This corresponds to twice the maximum energy Ω_0 of the acoustic phonons, which, within our phenomenological model, disperse linearly in the momentum range of interest. Therefore, $\Omega_0 \equiv c_s k_{cut}$, where $c_s \sim 5.0 \cdot 10^3 \text{ ms}^{-1}$ is the speed of sound in LAO. At this stage, Ω_0 is a free parameter, as we are not able to determine k_{cut} experimentally nor theoretically.

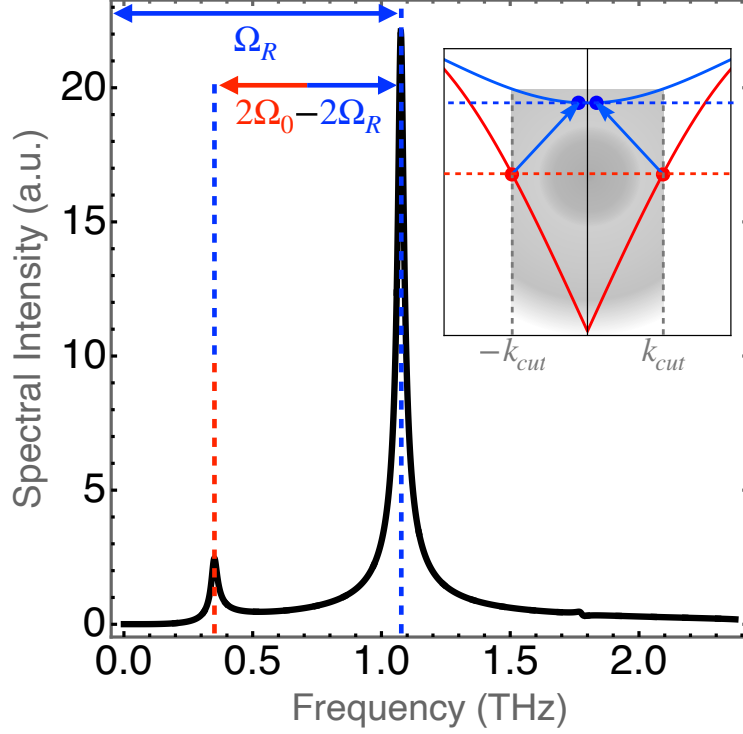


Figure 3. **Theoretical modeling of the parametric phonon dynamics in LaAlO_3 .** Spectral intensity of the Raman amplitude $|x|$ (solid black line). Blue and red colors denote features of the Raman-active and acoustic phonons, respectively. The mixed blue-red line indicates the subharmonic peak resulting from parametric driving of the Raman-active phonon by acoustic phonons. The inset illustrates the two dispersions and the up-conversion mechanism: two acoustic phonons (red dots) convert into two Raman-active phonons (blue dot). The gray-shaded area represents the effective momentum and frequency range for up-conversion coupling, significantly enhanced at $\pm k_{cut}$, when acoustic phonons have energy Ω_0 .

Setting $k_{cut} \sim 0.0142 \text{ \AA}^{-1}$, so that $k_{cut} \ll k_D$, we get $\Omega_0 \sim 0.71 \text{ THz}$. With these values of k_{cut} and Ω_0 , we can reproduce the subharmonic peak at 0.34 THz.

As detailed in the Supplementary Information, δ scales as $1/\Omega_{pump}^2$. This means that for the 1300 nm pump field, $\delta \sim 0$, and thus Eq. (2) describes a simple harmonic motion with frequency Ω_R , in agreement with the experimental findings. For the THz pump field δ is finite and, according to Eq. (2), the Raman-active mode undergoes, under very general initial conditions, a non-trivial periodic motion that can be analyzed in the frequency domain through the Fourier transform $x(\Omega) = \int dt e^{i\Omega t} x(t)$ of the coordinate $x(t)$.

The frequency-dependent coordinate $x(\Omega)$ exhibits a prominent spectral component at the Raman characteristic frequency Ω_R ($\Omega = 1$ in rescaled units), accompanied by smaller components either above (harmonic components) or below (sub-harmonic components) $\Omega = 1$, depending on the value of ω . To gain deeper insight into these features, we notice that Eq. (2) defines a Floquet dynamical system with a characteristic period $T \equiv 2\pi/\omega$ [39]. This allows for stable solutions that can be expanded in Fourier series as $x(t) = \sum_n c_n e^{i(1+n\omega)t}$, where a finite value of c_n indicates that a peak at $\Omega = 1 + n\omega$ appears in the spectrum of $x(\Omega)$. In the non-resonant case, in which Ω_0 is not equal to Ω_R , two main regimes can be distinguished: above and below $\omega = 2$. When $\omega > 2$, spectral components are present only at $\Omega = 1$ or higher frequencies, whereas when $\omega < 2$, one has, e.g., that the Fourier component at $n = -1$, with frequency $\Omega = \omega - 1$, is a sub-harmonic of the main one, since $\omega - 1 < 1$. In general, for $1 < \omega < 2$ a unique sub-harmonic component at $\Omega = \omega - 1$ emerges, while below $\omega = 1$ there are $N \geq 2$ sub-harmonics when ω lies in the interval $\frac{2}{N+1} < \omega < \frac{2}{N}$. In the present case we assumed an ultrashort pump pulse, and as such the spectral components are solely determined by twice the acoustic-phonon frequency $2\Omega_0$, with the positions of the peaks remaining unchanged when the pump frequency is adjusted. The experimental findings strongly support this general physical picture. Nevertheless, as we discuss in detail in the Supplementary, the physical scenario in the case of a narrow-band pump is very similar, hence the validity of our approach general and independent on these details.

In order to directly compare the theoretical expectations with the experiment, we show the spectral amplitude $|x(\Omega)|$ as a function of Ω in Fig. 3. To solve Eq. (2), we estimate $\delta = 0.2$ (see Supplementary Information), include a damping term $2\gamma\dot{x}(t)$ with $\gamma = 0.01$, evaluated by observing the decay of oscillations at $\Omega = 1$ in the time domain, and set the initial condition as $x(0) = 0$, $\dot{x}(0) = v_0$, where v_0 is linked to the ISRS. Since $\Omega_R \sim 1.08$ THz and $\Omega_0 \sim 0.71$ THz, the parametric driving occurs at $\omega \sim 1.31$, so we expect a single sub-harmonic peak at $\Omega \sim 0.31$ (i.e., 0.34 THz), regardless of the pump frequency. This prediction is consistently supported by the experimental findings.

In conclusion, we have presented evidences for occurrence of phononic parametric driving of a Raman active mode through the coupling of an intense terahertz pulses with acoustic waves. The resulting form of acoustic-optical interaction can explain a physical scenario in which the Raman mode is coherently excited and it is accompanied by the creation

of dynamical components at subharmonic frequencies. Specifically, the ability to induce oscillating modes at lower frequencies of the Raman mode is a defining characteristic of the observed phenomenon. The implications of our findings are generally vast, ranging from energy harvesting technologies to the development of new sensors and communication devices. At a fundamental level, our findings pave the way for new advancements in the field of parametric-driven phononics.

-
- [1] L. Landau and E. Lifshitz, *Mechanics* (Butterworth-Heinemann, 1976).
 - [2] M. A. Castellanos-Beltran, K. D. Irwin, G. C. Hilton, L. R. Vale, and K. W. Lehnert, Amplification and squeezing of quantum noise with a tunable Josephson metamaterial, *Nature Physics* **4**, 929 (2008).
 - [3] C. Macklin, K. O’Brien, D. Hover, M. E. Schwartz, V. Bolkhovskiy, X. Zhang, W. D. Oliver, and I. Siddiqi, A near quantum-limited Josephson traveling-wave parametric amplifier, *Science* **350**, 307 (2015).
 - [4] P. Krantz, A. Bengtsson, M. Simoen, S. Gustavsson, V. Shumeiko, W. D. Oliver, C. M. Wilson, P. Delsing, and J. Bylander, Single-shot read-out of a superconducting qubit using a josephson parametric oscillator, *Nature Communications* **7**, 11417 (2016).
 - [5] S. Harris, Tunable optical parametric oscillators, *Proceedings of the IEEE* **57**, 2096 (1969).
 - [6] L. E. Myers, R. C. Eckardt, M. M. Fejer, R. L. Byer, W. R. Bosenberg, and J. W. Pierce, Quasi-phase-matched optical parametric oscillators in bulk periodically poled LiNbO₃, *J. Opt. Soc. Am. B* **12**, 2102 (1995).
 - [7] R. A. Leenders, D. Afanasiev, A. V. Kimel, and R. V. Mikhaylovskiy, Canted spin order as a platform for ultrafast conversion of magnons, *Nature* **630**, 335 (2024).
 - [8] P. L. McMahon, A. Marandi, Y. Haribara, R. Hamerly, C. Langrock, S. Tamate, T. Inagaki, H. Takesue, S. Utsunomiya, K. Aihara, R. L. Byer, M. M. Fejer, H. Mabuchi, and Y. Yamamoto, A fully programmable 100-spin coherent Ising machine with all-to-all connections, *Science* **354**, 614 (2016).
 - [9] B. Yurke, P. G. Kaminsky, R. E. Miller, E. A. Whittaker, A. D. Smith, A. H. Silver, and R. W. Simon, Observation of 4.2-K equilibrium-noise squeezing via a Josephson-parametric amplifier, *Phys. Rev. Lett.* **60**, 764 (1988).

- [10] R. Schnabel, Squeezed states of light and their applications in laser interferometers, *Physics Reports* **684**, 1 (2017), squeezed states of light and their applications in laser interferometers.
- [11] G. Breitenbach, S. Schiller, and J. Mlynek, Measurement of the quantum states of squeezed light, *Nature* **387**, 471 (1997).
- [12] M. Först, C. Manzoni, S. Kaiser, Y. Tomioka, Y. Tokura, R. Merlin, and A. Cavalleri, Non-linear phononics as an ultrafast route to lattice control, *Nature Physics* **7**, 854 (2011).
- [13] N. Li, J. Ren, L. Wang, G. Zhang, P. Hänggi, and B. Li, Colloquium: Phononics: Manipulating heat flow with electronic analogs and beyond, *Rev. Mod. Phys.* **84**, 1045 (2012).
- [14] A. Subedi, A. Cavalleri, and A. Georges, Theory of nonlinear phononics for coherent light control of solids, *Phys. Rev. B* **89**, 220301 (2014).
- [15] D. M. Juraschek, M. Fechner, and N. A. Spaldin, Ultrafast structure switching through nonlinear phononics, *Phys. Rev. Lett.* **118**, 054101 (2017).
- [16] A. A. Balandin, Phononics of graphene and related materials, *ACS Nano* **14**, 5170 (2020).
- [17] S. Wallentowitz, W. Vogel, I. Siemers, and P. E. Toschek, Vibrational amplification by stimulated emission of radiation, *Phys. Rev. A* **54**, 943 (1996).
- [18] K. Vahala, M. Herrmann, S. Knünz, V. Batteiger, G. Saathoff, T. W. Hänsch, and T. Udem, A phonon laser, *Nature Physics* **5**, 682 (2009).
- [19] M. Ip, A. Ransford, A. M. Jayich, X. Long, C. Roman, and W. C. Campbell, Phonon lasing from optical frequency comb illumination of trapped ions, *Phys. Rev. Lett.* **121**, 043201 (2018).
- [20] R. M. Pettit, W. Ge, P. Kumar, D. R. Luntz-Martin, J. T. Schultz, L. P. Neukirch, M. Bhattacharya, and A. N. Vamivakas, An optical tweezer phonon laser, *Nature Photonics* **13**, 402 (2019).
- [21] I. S. Grudinin, H. Lee, O. Painter, and K. J. Vahala, Phonon laser action in a tunable two-level system, *Phys. Rev. Lett.* **104**, 083901 (2010).
- [22] T. F. Nova, A. Cartella, A. Cantaluppi, M. Först, D. Bossini, R. V. Mikhaylovskiy, A. V. Kimel, R. Merlin, and A. Cavalleri, An effective magnetic field from optically driven phonons, *Nature Physics* **13**, 132 (2017).
- [23] D. L. Chafatinos, A. S. Kuznetsov, S. Anguiano, A. E. Bruchhausen, A. A. Reynoso, K. Biermann, P. V. Santos, and A. Fainstein, Polariton-driven phonon laser, *Nature Communications* **11**, 4552 (2020).
- [24] R. P. Beardsley, A. V. Akimov, M. Henini, and A. J. Kent, Coherent terahertz sound am-

- plification and spectral line narrowing in a stark ladder superlattice, *Phys. Rev. Lett.* **104**, 085501 (2010).
- [25] A. Cartella, T. F. Nova, M. Fechner, R. Merlin, and A. Cavalleri, Parametric amplification of optical phonons, *Proceedings of the National Academy of Sciences* **115**, 12148 (2018).
 - [26] M. V. Klein, *Electronic Raman scattering* (Springer, 2005) pp. 147–204.
 - [27] A. Maradudin and R. Wallis, Ionic Raman effect. i. scattering by localized vibration modes, *Physical Review B* **2**, 4294 (1970).
 - [28] R. Wallis and A. Maradudin, Ionic Raman effect. ii. the first-order ionic Raman effect, *Physical Review B* **3**, 2063 (1971).
 - [29] L. Humphreys, Ionic Raman effect. iii. first-and second-order ionic Raman effects, *Physical Review B* **6**, 3886 (1972).
 - [30] M. Först, C. Manzoni, S. Kaiser, Y. Tomioka, Y.-n. Tokura, R. Merlin, and A. Cavalleri, Nonlinear phononics as an ultrafast route to lattice control, *Nature Physics* **7**, 854 (2011).
 - [31] G. Khalsa, N. A. Benedek, and J. Moses, Ultrafast control of material optical properties via the infrared resonant Raman effect, *Physical Review X* **11**, 021067 (2021).
 - [32] M. Coll, J. Fontcuberta, M. Althammer, M. Bibes, H. Boschker, A. Calleja, G. Cheng, M. Cuoco, R. Dittmann, B. Dkhil, I. El Baggari, M. Fanciulli, I. Fina, E. Fortunato, C. Frontera, S. Fujita, V. Garcia, S. Goennenwein, C.-G. Granqvist, J. Grollier, R. Gross, A. Hagfeldt, G. Herranz, K. Hono, E. Houwman, M. Huijben, A. Kalaboukhov, D. Keeble, G. Koster, L. Kourkoutis, J. Levy, M. Lira-Cantu, J. MacManus-Driscoll, J. Mannhart, R. Martins, S. Menzel, T. Mikolajick, M. Napari, M. Nguyen, G. Niklasson, C. Paillard, S. Panigrahi, G. Rijnders, F. Sánchez, P. Sanchis, S. Sanna, D. Schlom, U. Schroeder, K. Shen, A. Siemon, M. Spreitzer, H. Sukegawa, R. Tamayo, J. van den Brink, N. Pryds, and F. M. Granozio, Towards oxide electronics: a roadmap, *Applied Surface Science* **482**, 1 (2019).
 - [33] A. J. Hatt and N. A. Spaldin, Structural phases of strained LaAlO_3 driven by octahedral tilt instabilities, *Physical Review B* **82**, 195402 (2010).
 - [34] S. Kustov, I. Liubimova, and E. Salje, LaAlO_3 : A substrate material with unusual ferroelastic properties, *Applied Physics Letters* **112** (2018).
 - [35] H. Yokota, C. Haines, S. Matsumoto, N. Hasegawa, M. A. Carpenter, Y. Heo, A. Marin, E. Salje, and Y. Uesu, Domain wall generated polarity in ferroelastics: Results from resonance piezoelectric spectroscopy, piezoelectric force microscopy, and optical second harmonic

- generation measurements in LaAlO_3 with twin and tweed microstructures, *Physical Review B* **102**, 104117 (2020).
- [36] F. D. Brunner, O.-P. Kwon, S.-J. Kwon, M. Jazbinšek, A. Schneider, and P. Günter, A hydrogen-bonded organic nonlinear optical crystal for high-efficiency terahertz generation and detection, *Optics express* **16**, 16496 (2008).
 - [37] M. Abrashev, A. Litvinchuk, M. Iliev, R. Meng, V. Popov, V. Ivanov, R. Chakalov, and C. Thomsen, Comparative study of optical phonons in the rhombohedrally distorted perovskites LaAlO_3 and LaMnO_3 , *Physical Review B* **59**, 4146 (1999).
 - [38] Y. Liu, A. Frenkel, G. Garrett, J. Whitaker, S. Fahy, C. Uher, and R. Merlin, Impulsive light scattering by coherent phonons in LaAlO_3 : Disorder and boundary effects, *Physical review letters* **75**, 334 (1995).
 - [39] G. Acar and B. F. Feeny, Floquet-based analysis of general responses of the mathieu equation, *Journal of Vibration and Acoustics* **138**, 041017 (2016).
 - [40] Y. Hu, C. Zhang, J. Shen, and X. Zhang, Time-domain terahertz spectroscopy of (100) MgO and (100) LaAlO_3 substrates, *Acta Physica Sinica* **53**, 1772 (2004).
 - [41] M. Udina, T. Cea, and L. Benfatto, Theory of coherent-oscillations generation in terahertz pump-probe spectroscopy: From phonons to electronic collective modes, *Phys. Rev. B* **100**, 165131 (2019).
 - [42] F. Gabriele, M. Udina, and L. Benfatto, Non-linear terahertz driving of plasma waves in layered cuprates, *Nature Communications* **12**, 752 (2021).
 - [43] J. Fiore, N. Sellati, F. Gabriele, C. Castellani, G. Seibold, M. Udina, and L. Benfatto, Manipulating plasma excitations with terahertz light pulses in superconducting cuprates, *arXiv preprint arXiv:2310.16815* (2023).
 - [44] M. Basini, M. Udina, M. Pancaldi, V. Unikandanunni, S. Bonetti, and L. Benfatto, Terahertz ionic kerr effect: two-phonon contribution to the nonlinear optical response in insulators, *Physical Review B* **109**, 024309 (2024).

Data availability

The data that support the findings of this study are available from the corresponding authors on request.

Code availability

The code that supports the findings of the study is available from the corresponding authors on request.

Acknowledgements

M.B., V.U., and S.B. acknowledge support from the Knut and Alice Wallenberg Foundation (Grant No. 2019.0068). M.Cu. acknowledges support from the EU's Horizon 2020 research and innovation program under Grant Agreement No. 964398 (SUPERGATE) and from PNR MUR project PE0000023-NQSTI. F.F. and F.G. acknowledge support by the Italian Ministry of University and Research (MIUR), under grant PON 2020JZ5N9M. We gratefully acknowledge discussions with G. Khalsa and S.L.Jhonson (others?).

Contributions

M.B., V.U. and F.G. contributed equally to this manuscript M.B. and V.U. performed the experiments with terahertz spectroscopy. M.Cu., F.F. and F.G. conceived the idea of the parametric excitation and developed the theoretical model. F.G. performed the computational analysis with support from F.F and M.Cu. M.Cr. and M.C.H. performed independent experiments to support the main experimental findings. S.B. devised the project with the help of all the authors, and coordinated it. M.B., V.U., F.G. and M.Cu. and S.B. wrote the manuscript. All the authors discussed the results and their interpretation and revised the manuscript.

Corresponding authors

Correspondence and requests for materials should be addressed to Stefano Bonetti.

Ethics declarations

The authors declare no competing interests.

Supplementary Information

I. THZ TIME-DOMAIN SPECTROSCOPY

Here we show a static characterization (THz Time Domain Spectroscopy, THz-TDS) of the LAO sample, performed at 8K in transmission geometry. To generate a comparable field profile and amplitude to the pump-probe experiment, the incident THz field was generated in the same experimental configuration (1300nm rectification in an organic OH1 crystal). The scientific motivation is to investigate possible contributions due to the Eg phonon in the complex refractive index. Figure S1.a shows the sample transmittance defined as E_T/E_I , where E_T and E_I are the transmitted and incident fields respectively. The transmitted THz shows no absorption at 1.08 THz confirming the Raman activity of the Eg mode. The calculated complex refractive index is shown in figure S1.b and it is consistent with previously reported data [40]. It is worth noticing that even if we show here data associated with an incident field amplitude of $E_{THz} = 550\text{kV/cm}$, we obtained the same evidence in the amplitude range $20\text{ kV/cm} < E_{THz} < 550\text{ kV/cm}$.

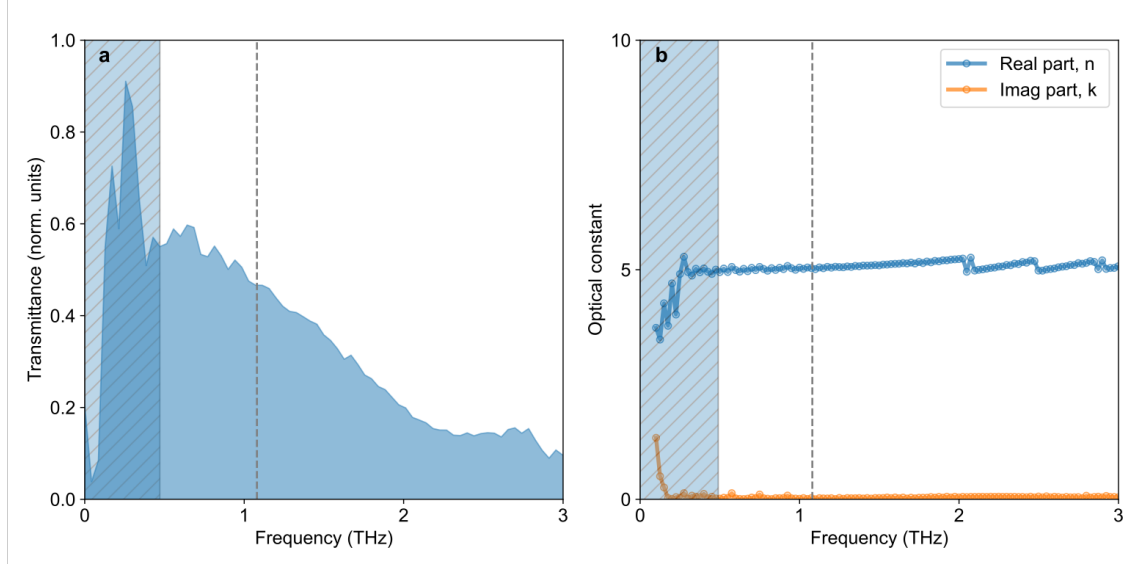


Figure S1. THz-TDS on LaAlO₃ [100] sample, the incident field is the same as the pumping field of Figure 2. The field amplitude is 550kV/cm.

II. PUMP-PROBE RESPONSE WITH 1 AND 2 THZ PUMP

In order to investigate the excitation mechanism in the case of the terahertz pulses, we additionally produce narrowband fields from the broadband terahertz pulses inserting 1 THz and, respectively, 2 THz band-pass filters before the sample. The time trace of the narrowband THz is shown in Fig. S2(a), with light blue lines representing the excitation centered at 1 THz, and light orange lines indicating the one at around 2 THz. The corresponding Fourier transforms are displayed in Fig. S2(b). The two narrowband terahertz pumps are designed so to have approximately the same field strength for a quantitative comparison. The inset in panel (b) shows that the peak associated with the E_g mode scales with the square of the pump field amplitude, which suggests an IRSR driving mechanism of the Raman-active phonon.

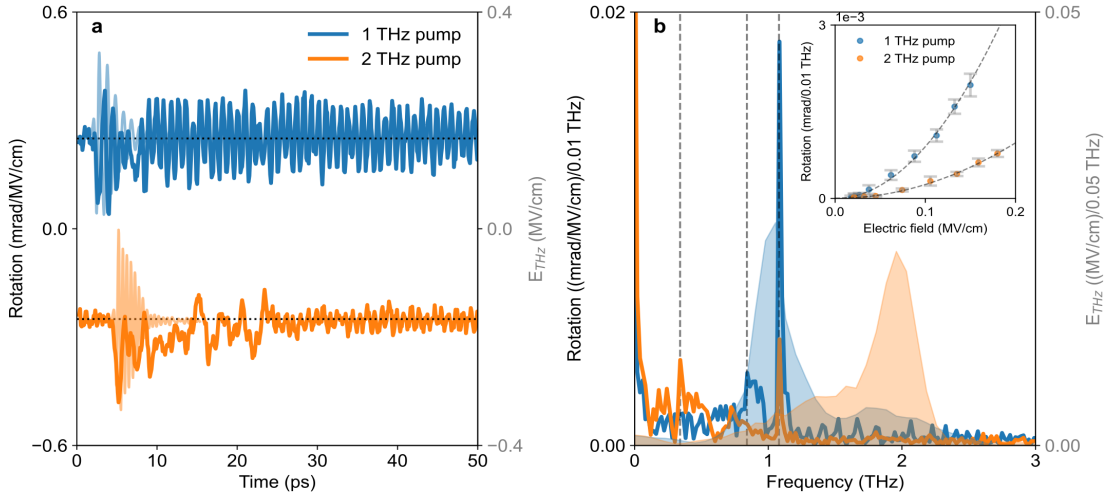


Figure S2. $\text{LaAlO}_3[100]$ Probe polarization rotation in time (a) and frequency domain (b) following narrowband THz excitation (with central frequencies of 1 THz and 2 THz). The light blue and orange traces in panel (a), as well as the light blue and orange shaded regions in panel (b), show electro-optical sampling of the incident narrowband THz pulses in the time and frequency domains, respectively. Inset of panel (b) shows E_g amplitude vs electric field amplitude. The dashed gray lines in the inset show the best fit

III. TIME-FREQUENCY ANALYSIS OF THE (THZ)PUMP-PROBE RESPONSE

We show a time frequency analysis of the signals shown in Figure 2 in the main text. The analysis in panel (a) shows the low-frequency components starting before the activation Eg mode.

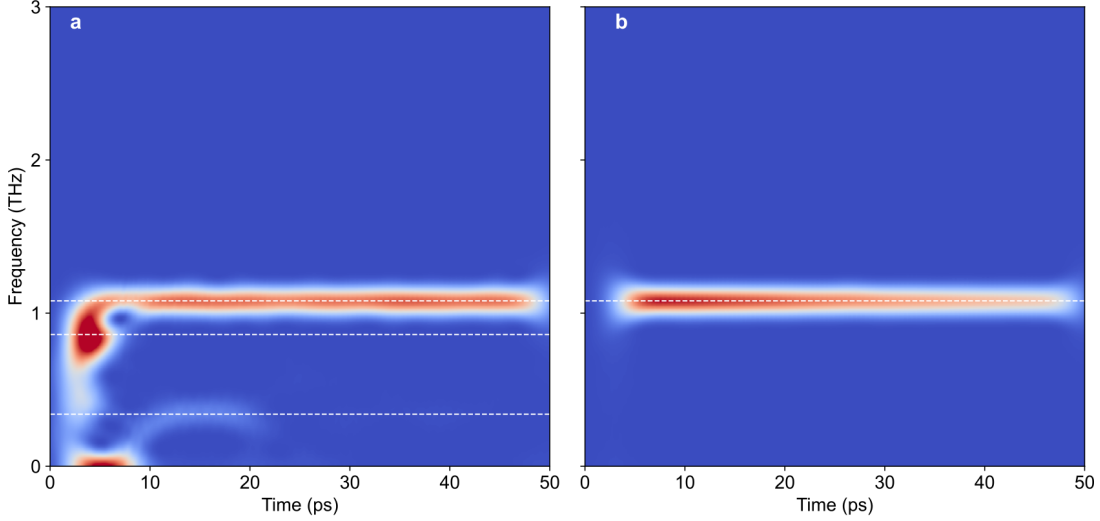


Figure S3. Time frequency analysis of the sample's response to a THz (a) and 1300nm (b) pumping field. A window of 8 ps was applied.

IV. EFFECTIVE RAMAN-ACTIVE PHONON DYNAMICS

In this section we derive the quantum correction to the quadratic action of the Raman-active phonon Q_R , showing that integrating out the acoustic phonons at one-loop approximation amounts to a parametric driving of the Raman-active mode itself. One starts from the total action (with $\hbar = 1$)

$$S[Q_R, Q_{ac}] = S_G^R[Q_R] + S_G^{ac}[Q_{ac}] + S_{R+ac}[Q_R, Q_{ac}]. \quad (\text{S1})$$

The first two contributions are the Gaussian actions of the Raman-active and the acoustic phonons, that read, in momentum space,

$$S_G^R[Q_R] = \frac{1}{2} \sum_{\mathbf{k}} \int d\omega (\omega^2 - \Omega_R^2) Q_R(-\mathbf{k}, -\omega) Q_R(\mathbf{k}, \omega), \quad (\text{S2})$$

$$S_G^{ac}[Q_{ac}] = \frac{1}{2} \sum_{\mathbf{k}} \int d\omega [\omega^2 - \Omega_{ac}^2(\mathbf{k})] Q_{ac}(-\mathbf{k}, -\omega) Q_{ac}(\mathbf{k}, \omega), \quad (\text{S3})$$

where, as already discussed in the main text, the sum runs over momenta close to the Γ point, where Ω_R has a rather flat dispersion and does not depend on the momentum \mathbf{k} . The last contribution describes the coupling of the acoustic phonons with the external field and the acousto-optic conversion, i.e.,

$$\begin{aligned} S_{R+ac}[Q_R, Q_{ac}] &= \frac{Z_{ac}}{2} \sum_{\mathbf{k}} \int \frac{d\omega d\omega'}{\sqrt{2\pi}} Q_{ac}(-\mathbf{k}, -\omega) Q_{ac}(\mathbf{k}, \omega') E_{ext}^2(\omega - \omega') \\ &\quad - \frac{d}{4} \frac{1}{\sqrt{N_{\mathbf{k}}}} \sum_{\mathbf{k}, \mathbf{k}'} \int \frac{d\omega d\omega'}{\sqrt{2\pi}} Q_{ac}(-\mathbf{k}, -\omega) Q_{ac}(\mathbf{k}', \omega) Q_R^2(\omega - \omega', \mathbf{k} - \mathbf{k}'), \end{aligned} \quad (\text{S4})$$

where $N_{\mathbf{k}}$ is the effective number of sites in \mathbf{k} -space,

$$E_{ext}^2(\omega) = \left(\frac{E_0}{2} \right)^2 [2F^2(\omega) + F^2(\omega - 2\Omega_{pump}) + F^2(\omega + 2\Omega_{pump})] \quad (\text{S5})$$

is the pump field in the frequency domain, with $F^2(\omega) = \int \frac{d\omega}{\sqrt{2\pi}} e^{i\omega t} F^2(t)$ the Fourier transform of the squared envelope function, and Q_R^2 stands for the convolution product $Q_R^2(\omega, \mathbf{q}) = \frac{1}{\sqrt{N_{\mathbf{k}}}} \sum_{\mathbf{k}'} \int \frac{d\omega'}{\sqrt{2\pi}} Q_R(\omega - \omega', \mathbf{q} - \mathbf{k}') Q_R(\omega', \mathbf{k}')$. In order to derive the effective action for Q_R we notice that in the sector of the total action that contains the acoustic phonons one can identify a diagonal and a non-diagonal contribution that are, respectively,

$$D^{-1}(\mathbf{k}, \omega) \equiv \omega^2 - \Omega_{ac}^2(\mathbf{k}), \quad (\text{S6})$$

i.e., the acoustic phonon propagator, and

$$R(\omega - \omega', \mathbf{k} - \mathbf{k}') = \frac{Z_{ac}}{\sqrt{2\pi}} E_{ext}^2(\omega - \omega') \delta^{(3)}(\mathbf{k} - \mathbf{k}') - \frac{1}{\sqrt{2\pi N_{\mathbf{k}}}} \frac{d}{2} Q_R^2(\omega - \omega', \mathbf{k} - \mathbf{k}'), \quad (\text{S7})$$

so that $S_G^{(ac)}[Q_{ac}] + S_{R+ac}[Q_R, Q_{ac}] = (1/2) \sum_{k, k'} [D^{-1}(k) \delta_{k, k'} + R(k, k')] Q_{ac}(-k) Q_{ac}(k')$, with $k \equiv (\mathbf{k}, i\Omega_m)$ and $\sum_k \equiv \sum_{\mathbf{k}} \int d\omega$. By standard computations[41–44], one integrates out the acoustic phonons at one-loop approximation and then makes an expansion in the non-diagonal term R , that yields, at one-loop approximation,

$$\begin{aligned} &\frac{\hbar}{2} \sum_k \sum_q D(k+q) D(q) R(k) R(-k) \\ &= \sum_{\mathbf{k}} \int dt Q_R(t, -\mathbf{k}) Q_R(t, \mathbf{k}) \int \frac{d\omega}{\sqrt{2\pi}} e^{-i\omega t} K(\omega) E_{ext}^2(\omega) \end{aligned} \quad (\text{S8})$$

where we made \hbar explicit again and the kernel K reads, in the low-temperature limit $T \rightarrow 0$ [42]:

$$K(\omega) = \frac{K_0}{N_{\mathbf{k}}} \sum_{\mathbf{k}} \frac{1}{\Omega_{ac}(\mathbf{k})} \frac{1}{4\Omega_{ac}^2(\mathbf{k}) - (\omega + i0^+)^2} \quad (\text{S9})$$

where $K_0 \equiv \hbar(Z_{ac}d)/2$ and $i0^+$ is the vanishing positive imaginary part that guarantees causality. To proceed further, we distinguish between two limiting cases, the one of a narrow-band monochromatic pump field, for which the time-domain envelope function $F(t) = 1$ is constant, $F^2(\omega) = \sqrt{2\pi}\delta(\omega)$ and $E_{ext}^2(\omega)$ exhibits three sharp peaks at $\omega = 0, \pm 2\Omega_{pump}$, and the case of a broad-band pump with an ultrashort lifetime $F(t) \sim \sqrt{2\pi}\tau\delta(t)$ in time-domain, with τ the pulse duration, and a flat $F(\omega)^2 \sim \tau/\sqrt{2}$ profile in frequency domain. In the former case the frequency dependence of $K(\omega)E_{ext}^2(\omega)$ in Eq. S8 is dominated by the delta-like peaks of the squared pump field, and one gets that $\int \frac{d\omega}{\sqrt{2\pi}} e^{-i\omega t} K(\omega)E_{ext}^2(\omega) = \frac{\sqrt{2\pi}E_0^2}{2} |K(2\Omega_{pump})| \sin(2\Omega_{pump}t + \phi)$, with $\phi \equiv \arctan\left(\frac{K'(2\Omega_{pump})}{K''(2\Omega_{pump})}\right)$, K' and K'' being the real and imaginary part of the kernel, i.e., the one-loop correction amounts to a parametric driving of the Raman-active phonon at *twice* the pump frequency. In the latter case the integral in Eq. S8 equals, for $t > 0$,

$$\begin{aligned} \int \frac{d\omega}{\sqrt{2\pi}} e^{-i\omega t} K(\omega)E_{ext}^2(\omega) &= \frac{K_0 E_0^2 \tau}{2\sqrt{\pi}} \frac{1}{N_{\mathbf{k}}} \sum_{\mathbf{q}} \frac{1}{2\Omega_{ac}^2(\mathbf{q})} \sin(2\Omega_{ac}(\mathbf{q})t) \\ &= \frac{K_0 E_0^2 \tau}{2\sqrt{\pi}} \int dz \rho(z) \frac{\sin(zt)}{2z^2} \sim \frac{3K_0 E_0^2 \tau}{4\sqrt{\pi}\Omega_0^2} \sin(2\Omega_0 t), \end{aligned} \quad (\text{S10})$$

where the density of states of acoustic phonons, that is a monotonic increasing function of ω , is approximated by a sharp-peaked delta distribution around the maximum acoustic-phonon frequency Ω_0 , i.e.,

$$\rho_{ac}(z) \sim 3\delta(z - \Omega_0), \quad (\text{S11})$$

with the overall prefactor 3 accounting for all acoustic-phonon branches. One then gets a parametric driving of the Raman-active phonon at *twice* the frequency of the acoustic phonons for $t > 0$, regardless of the pump frequency. The parametric-driving of the Raman-active phonon can be then incorporated by adding the following contribution to the total potential,

$$V_{para}(Q_R) = C(\Omega_{pump}, \Omega_0) \cos(2\Omega_0 t) \sum_{\mathbf{k}} Q_R(-\mathbf{k}, t) Q_R(\mathbf{k}, t), \quad (\text{S12})$$

where $C(\Omega_{pump}, \Omega_0) \equiv \frac{3\sqrt{2\pi}K_0}{2} \frac{E_0^2 \tau}{\Omega_0^2}$. Now, in order to get a numerical value for the driving parameter $\delta \equiv C/\Omega_0^2$ in Eq. 2, we estimate the coefficients d and Z_{ac} by assuming a simplified

situation in which the system is a diatomic 1-D chain, with a lattice spacing $a \sim 3.0 \text{ \AA}$, of alternating oxygen and aluminum ions that interact via a nearest-neighbour Yukawa-like potential $V(x) = k_e^{LAO} (Z_O Z_{Al} e^2) e^{-\mu x}/x$, where $k_e^{LAO} \sim 6 \cdot 10^2 \text{ meV \AA}$ is the Coulomb constant in LAO, $Z_O^* \sim 4.55$ and $Z_{Al}^* \sim 3$ are the effective charges of oxygen and aluminum and μ is the inverse attenuation length. From the expression of the optical Raman-active phonon frequency at $\mathbf{k} \sim \mathbf{0}$, i.e. $\Omega_R \sim \sqrt{2V''(a)(M_O + M_{Al})(M_O M_{Al})}$, we extract $\mu \sim 2.22 \text{ \AA}^{-1}$, and we can thus estimate $d \sim V^{(4)}(a)/(M_O M_{Al}) \sim 0.4 \text{ meV \AA}^{-4} \text{ amu}^{-2}$. To estimate the effective charge associated with the excitation of the two acoustic photons we perform the Peierls substitution $k \rightarrow k - \frac{e}{\hbar c} A(t)$ inside the acoustic-phonon frequency, with $A(t)$ the vector potential such that $E(t) = -(1/c)\partial_t A(t)$. The effective charge then scales with the second derivative of the acoustic-phonon frequency, i.e. $Z_{ac} \sim \omega_{ac}''(0)/(\hbar\Omega_{pump})^2 \sim 0.3 \text{ meV}^{-1} \text{ amu}^{-1}$. Then, setting $\Omega_0 \sim 0.71 \text{ THz}$ as discussed in the main text, and taking into account the parameters of e.g. the 1-THz experimental pump $E_0 \sim 1.5 \text{ mV \AA}^{-1}$ and $\tau \sim 5 \text{ ps}$, we obtain the estimate $\delta \sim 0.2$ for the driving parameter.

We now briefly discuss the role of the ISRS, that enters the right-hand side of Mathieu Eq. as a direct driving on the Raman-active phonon, i.e.

$$\ddot{x}(t) + [1 + \delta \cos(\omega t)] x(t) = \alpha E^2(t), \quad (\text{S13})$$

where $\alpha = R/\Omega_R^2$, with R the Raman tensor[38]. For an ultrashort pump with an envelope such that $F^2(t) \sim \sqrt{\pi/2}\delta(t)$, Eq. (S13) is equivalent to an undriven Mathieu Eq. with initial conditions $x(0^+) = 0$ and $\dot{x}(0^+) = v_0$, where $v_0 \equiv \sqrt{\pi} R E_0^2 / (2\Omega_R^2)$: indeed, for $t > 0$, $E(t) = 0$; furthermore, by integrating both sides of Eq. (S13) twice over an infinitesimal interval $[-dt, dt]$ around $t = 0$ and considering that the oscillator is at rest for $t < 0$ (i.e., $x(0^-) = 0$ and $\dot{x}(0^-) = 0$), we find the initial conditions mentioned above by taking the limit $dt \rightarrow 0^+$.